1 Title page

2 **Effect of colloidal particle size on physicochemical properties**

3 **and aggregation behaviors of two alkaline soils**

4 Yu-yang Yan[1], Xin-ran Zhang[1], Chen-yang Xu[1,2]*, Jun-jun Liu[1], Fei-nan

5 Hu[3,4], Zeng-chao Geng[1,2]

6 (1. *College of Natural Resources and Environment, Northwest A&F University,*

7 *Yangling, Shaanxi 712100, China*; 2. *Key Laboratory of Plant Nutrition and the Agri-*

8 *environment in Northwest China, Ministry of Agriculture, Northwest A&F University,*

9 *Yangling, Shaanxi 712100, China; 3. State Key Laboratory of Soil Erosion and Dryland*

10 *Farming on the Loess Plateau, Northwest A&F University, Yangling, Shaanxi 712100,*

11 *China; 4. Institute of Soil and Water Conservation, Chinese Academy of Sciences,*

12 *Ministry of Water Resources, Yangling, Shaanxi 712100, China*)

13

14 ***Corresponding author:**

15 Chen-yang Xu

16 Email address: xuchenyang@nwafu.edu.cn, xuchenyang.ms@163.com;

17 Postal address: College of Natural Resources and Environment, Northwest

18 A&F University, No. 3 Taicheng Road, Yangling District, Shaanxi 712100,

19 China.

Abstract

Colloidal particles are the most active soil components, and they vary in elemental composition and environmental behaviors with the particle size due to the heterogenous nature of natural soils. The purposes of the present study are to clarify how particle size affects the physiochemical properties and aggregation kinetics of soil colloids, and to further reveal the underlying mechanisms. Soil colloidal fractions, from two alkaline soils—Anthrosol and Calcisol were subdivided into three ranges: $d < 2$ μm, $d < 1$ μm and $d < 100$ nm. The organic and inorganic carbon contents, clay mineralogy, surface electrochemical properties, including surface functional groups and zeta potentials, were characterized. Through time-resolved light scattering technique, the aggregation kinetics of soil colloidal fractions were investigated, and their critical coagulation concentrations (CCCs) were determined. With decreasing colloidal particle diameter, the total carbon content, organic carbon, organic functional groups content and illite content all increased. The zeta potential became less negative and the charge variability decreased with decreasing particle diameter. The CCC values of Anthrosol and Calcisol colloids followed the descending order of $d < 100$ nm, $d < 1$ μm, $d < 2$ μm. Compared with the course factions ($d < 1$ μm and $d < 2$ μm), soil nanoparticles were more abundant in organic carbon and more stable clay minerals ($d < 100$ nm), thus they exhibited strongest colloidal suspension stability. The differences in organic matter contents and clay mineralogy are the fundamental reasons for the differences in colloidal suspension stability behind the size effects of Anthrosol and Calcisol colloids. The present study revealed the size effects of two alkaline soil colloids on carbon content, clay minerals,

42   surface properties and suspension stability, emphasizing that soil nanoparticles are

43   prone to be more stably dispersed instead of being aggregated. These findings can

44   provide references for in-depth understanding of the environmental behaviors of the

45   heterogeneous soil organic-mineral complexes.

1. Introduction

Soils contain a series of solid particles in continuous sizes, ranging over six orders of magnitude from nanometers to millimeters (Lead and Wilkinson, 2006; Li et al., 2011), among which soil colloids are the most reactive fractions. Soil colloids are characterized by high surface area and abundant surface charges, exhibiting high potential for carbon sequestration and strong adsorption capacity, which can largely determine the fate and transport of pathogens, nutrients, heavy metals and organic pollutants, and might cause environmental problems to adjacent water bodies or groundwater (Baalousha et al., 2009; Calabi-Floody et al., 2011). Due to their high reactivity and fluidity in aqueous environment, soil colloids play an important role in physical, chemical and biogeochemical processes in natural environment (Schäfer et al., 2012; Mayordomo et al., 2016). The capacity of soil colloids in mobilizing bound nutrients and pollutants is closely related to their dispersion stability under various environmental conditions (Won and Burns, 2018). Therefore, studies on the dispersion stability of soil colloids have attracted extensive attention.

Currently, the definition of soil and environmental colloidal fractions is ambiguous. Soil colloidal fractions are defined as soil particles in diameter of < 1 μm (Lead and Wilkinson, 2006; Weil and Brady, 2016), and also being of < 2 μm (Zhang et al., 2021); while in some extreme cases, they can refer to the particles in diameter of 5–10 μm (Yin et al., 2010). Such discrepancies are seen among publications due to the fact that colloids are defined based on the particle diameter range within which they can display colloidal properties. Since for different materials, e.g., metal (Fe/Al/Ti) oxides, silica

70   gel, phyllosilicates, the specific colloidal range differs greatly.

71   Compared with engineered nanoparticles with known mineralogical organization,

72   natural soils are much more heterogeneous (Cárdenas et al., 2010); their elemental

73   composition and clay mineralogy of soil colloids change with particle size. Tsao et al.,

74   (2013) found that quartz and feldspar were mainly dominant in colloidal particles of <

75   2 μm and 450–2000 nm in red soil (Ferralsols, WRB, IUSS Working Group WRB.

76   2022), while illite and montmorillonite were the main clay minerals in nanoparticles

77   (1–100 nm). In addition, the mineral structure at nanometer scale also changes.

78   Compared with colloidal particles of < 2 μm, the Si/Al ratio in nanoparticles increased,

79   and the surface area, morphology, crystallinity, surface atomic structure and frame

80   structure were significantly different (Tsao et al., 2011). Furthermore, particle size also

81   affects the surface potential of soil colloids. Tang et al., (2015) investigated the surface

82   potential variations with particle size (1–10 μm, 0.5–1 μm, 0.2–0.5 μm, < 0.2 μm) for

83   variably-charged yellow soil (Lixisols) and permanently-charged purple soil

84   (Leptosols); among the colloidal fractions, the absolute surface potential of the finest

85   particles of purple soil (Leptosols) was lowest while that of the yellow soil (Lixisols)

86   was the largest, caused by the differences in surface charge density. Thus, the influences

87   of particle size on elemental composition and surface properties of soils should be

88   further studied.

89   In recent years, great progress has been made in the study of dispersion stability

90   of soil clay minerals, such as montmorillonite, kaolinite, illite or hematite, and soil

91   nanoparticles (Xu et al., 2018; Sun et al., 2020; Wei et al., 2021; Zhu et al., 2014). He

92 et al., (2008) demonstrated that hematite nanoparticles with various particle diameters

93 showed different surface properties and aggregation behaviors under the same pH

94 conditions; moreover, the critical coagulation concentrations (CCCs) of hematite

95 decreased with the decrease of particle diameter. Zhou et al., (2013) compared the

96 CCCs of ten different TiO_2 nanoparticles with varying sizes and indicated that crystal

97 structure and particle diameter both affected the aggregation behaviors of TiO_2. Zhang

98 et al. (2016) confirmed that the types of clay minerals for two Alfisols changed from

99 smectite and vermiculite to kaolinite and illite when the particle size varied from

100 colloids to nanoparticles. Therefore, the dependence of physiochemical properties,

101 surface properties and environmental behaviors on particle size for heterogeneous soil

102 colloidal particles needs systematic investigation.

103 In the present study, soil colloidal particles of two alkaline soils—Anthrosol and

104 Calcisol were subdivided into three ranges: $d < 2$ μm, $d < 1$ μm and $d < 100$ nm. Their

105 organic fraction and clay mineralogy, surface electrochemical properties and colloidal

106 stability were studied. This study selected two representative calcareous soils to verify

107 the following scientific hypothesis: soil colloids are organic-inorganic composites. As

108 particle diameter decreases (from colloid particles to nanoparticles), the number of

109 organic functional groups on the surface of soil colloids increases, and the type of clay

110 minerals shifts towards finer clay particles, e.g. illite, resulting in increased specific

111 surface area and decreased charge density, and thus enhanced suspension stability,

112 meaning particle diameter influences the composition of soil colloidal fractions,

113 thereby changing surface properties and suspension stability. The findings can have

important implications for predicting the environmental performances of colloids and colloid-facilitated nutrients, pollutes and pathogens in natural soil and water environment.

2. Materials and methods

2.1 Soil sampling

The study collected two surface soil samples (0–20 cm), Lou soil and Cinnamon soil, being calcareous soils, by mixing soils form 5–10 sampling points using a stainless-steel auger at Yangling District (N38°18′14″ and E108°2′30″), and Zhouzhi Country (N34°8′8″ and E108°3′10″), in Shaanxi province, northwest China, respectively. According to World Reference Base for Soil Resources (WRB, IUSS Working Group WRB. 2022), the Lou soil and Cinnamon soil are classified as Calcic Protocalcic Calcisols (Loamic, Lixic, Humic) and Hortic Endoanthric Anthrosols (Loamic, Luvic, Eutric, Calcic), respectively. Both types of soil developed from loess parent material. The typical soil profile configuration for the tested Anthrosol is Ap1-Ap2-Bt-Bk-C, while for the Calcisol, it is Ah-Bt-Bk-C.

Soils samples were taken back to laboratory for air-drying and sieving. The basic soil properties were determined based on standard methods. Soil pH was measured with a pH electrode, employing a solution-to-soil ratio of 2.5:1. Soil organic carbon (SOC) was determined using the $K_2Cr_2O_7$ oxidation method. The cation exchange capacity (CEC) of soil was measured with exchange method. The $CaCO_3$ content was determined by gasometric method. The free Fe/Al oxides were extracted by dithionite-citrate-bicarbonate (DCB) solution. The particle size distribution was measured using

136   the laser diffractometer of Malvern Mastersizer 2000 (Malvern Instruments Ltd., UK).

137   The pH of Anthrosol was 8.34 while it was 8.32 for the Calcisol. The SOC of Anthrosol

138   and Calcisol were 7.25 g·kg^{-1} and 9.22 g·kg^{-1}, respectively. The CEC of Anthrosol and

139   Calcisol were 25.9 cmol·kg^{-1} and 22.2 cmol·kg^{-1}.The contents of CaCO$_3$ in Anthrosol

140   and Calcisol were 51.7 g·kg^{-1} and 82.5 g·kg^{-1}. The Free Fe/Al oxides content of

141   Anthrosol and Calcisol were 22.8 g·kg^{-1} and 23.1 g·kg^{-1}. The proportions of Sand (2–

142   0.02 mm), Silt (0.02–0.002 mm) and Clay (<0.002 mm) in Anthrosol were 34.0%, 40.6%

143   and 25.4% while those were 28.0%, 44.8% and 27.2% for the Calcisol.

144   **2.2 Extraction of soil colloidal fractions in different size ranges**

145   The soil colloidal particles were extracted based on the Stokes' law, and the

146   detailed procedures can be found in our previous publication (Hu et al., 2022). Briefly,

147   50 g of dry soil was weighed into a beaker containing 500 mL of distilled water, and

148   put the suspension under sonication for an hour using the ultrasonic cell disrupter (XO-

149   900D, Nanjing Xianou Instruments Corporation, China) while maintaining the

150   temperature below 30°C. Afterwards, the suspension was transferred to a larger beaker

151   and distilled water was added to make up the total volume of 5 L. The suspension was

152   further dispersed using an electronic blade stirrer (JB-200, Shanghai Nanhui Huiming

153   Apparatus, China) for one hour, before being sieved through sieve with a pore size of

154   53 μm, and the upper suspensions containing soil colloidal particles in different

155   diameters were collected by centrifugation. Based on the equation (1), centrifugation

156   speed and time for colloidal particles of d < 2 μm, < 1 μm and < 100 nm were calculated

157   and shown in Table S1.

$$t = \frac{\eta \lg \frac{R_2}{R_1}}{3.81 N^2 r^2 \Delta d} \tag{1}$$

in which, t is time for centrifugation (s); R_1 is the distance from the surface of the liquid to the center of the axis of the centrifuge, here is 5.7 cm; R_2 is distance from the particles to the center of the axis of the centrifuge, here is 10.5 cm; N (rev·s^{-1}) is the centrifuge speed; r (cm) is the desired colloidal particle radius; Δd is the difference in density between the soil particles (2.65 g·cm^{-3}) and water (1 g·cm^{-3}), while Δd is 1.65 g·cm^{-3}; η is the water viscosity coefficient, here is 0.00839 g·cm^{-1}·s^{-1} at 25 °C.

2.3 Characterization of soil colloidal fractions in different size ranges

The initial particle diameters of soil colloids were determined by a time-resolved dynamic light scattering (DLS) apparatus (Nanobrook Omni, Brookhaven, USA). The organic carbon contents in soil colloids were determined by potassium dichromate external heating method and total carbon content was determined by elemental analyzer (Elementar Vario EL III, Germany). The inorganic carbon content was calculated by subtraction method (Wang et al., 2011). The clay mineralogy of soil colloids was determined by the XRD (Ultima-IV, Rigaku, Japan), and by comparing the intensity of the dominant X-ray diffraction peak of the soil mineral colloid to a standard mineral reference (Database ICDD 2004), the relative percentage content of the minerals was determined. The specific surface areas of the soil colloids were measured by BET-N$_2$ method (ASAP 2460, Micromeritics instrument, USA). High-resolution spectra of C1s and O1s of soil colloids were acquired by X-ray photoelectron spectroscopy (XPS) (Thermo Scientific K-Alpha, USA) (Luo et al., 2019), and the Gaussian−Lorentzian

179   curve-fitting program (XPSPEAK 4.1) was used to analyze the XPS spectra. The zeta

180   potentials of soil colloids were measured by Zeta PALS equipped with a BI-ZTU

181   Autotitrator (ZetaPALS, Brookhaven, USA) with 1 mmol·L^{-1} NaCl solution as the

182   background electrolyte; and the pH range of colloidal suspension was set to 3–10

183   adjusted with 0.1 mol·L^{-1} HCl and NaOH. The concentrations of K^+, Na^+, Ca^{2+}, and

184   Mg^{2+} in soil colloidal suspensions were measured by flame atomic absorption

185   spectrophotometry (PinAAciie 900F, USA).

186   **2.4 Aggregation kinetics of soil colloidal fractions**

187   The aggregation kinetic curves of soil colloidal particles in different electrolytes

188   were determined by time-resolved DLS measurements. The incident wavelength was

189   635 nm and the scattering angle was 90°. The stock colloidal suspensions with particle

190   concentration of 200 mg·L^{-1} were mixed with electrolyte solutions with equal volume.

191   The suspension pH was adjusted to 8.0, which was close to the pH value of natural soil

192   with addition of 0.1 mol·L^{-1} HCl or NaOH before measurement. The chosen electrolyte

193   concentrations for NaCl and $CaCl_2$ were 200–2000 and 2–20 mmol·L^{-1}. The effective

194   diameter (D_h) of the mixed sample was automatically recorded every 2 min, and an

195   aggregation kinetic curve was obtained in 30 min monitoring.

196   **2.5 Calculation of critical coagulation concentration**

197   According to the particle interaction theory, the aggregation kinetic curves under

198   electrolyte conditions can be divided into reaction-limited aggregation (RLA) stage

199   under low concentration which was affected by electrolyte conditions and diffusion-

200   limited aggregation (DLA) stage under high concentration which was not affected by

201   electrolyte concentration. The CCC is the critical electrolyte concentration when the

202   aggregation process changes from the RLA state ($\alpha < 1$) to the DLA state ($\alpha = 1$).

203   Attachment efficiency (α) represents the bonding probability of particle collisions and

204   can be calculated for each electrolyte concentration by using equation 2, which allowed

205   the curve of α as a function of electrolyte concentration to be plotted (Xu et al., 2020a;

206   Hu et al., 2022).

207
$$\alpha_{exp} = \frac{1}{W} = \frac{k_{11}}{\left(k_{11}\right)_{fast}} = \frac{\dfrac{1}{N_0}\left(\dfrac{da_h(t)}{dt}\right)_{t\to 0}}{\dfrac{1}{\left(N_0\right)_{fast}}\left(\dfrac{da_h(t)}{d_t}\right)_{t\to 0,\,fast}} \tag{2}$$

208   where D_h is the effective diameter of particles, t is the time (min); N_0 is the density of

209   particles; K_{11} is the aggregation rate of RLA; $(K_{11})_{fast}$ is the aggregation rate of DLA.

210   The intersection of RLA regime and DLA regime is the CCC.

211   The aggregation rates were calculated by the average of the last 5 effective

212   diameters divided by the aggregation time at specific electrolyte concentration. The

213   fractal dimension in the DLA regime was obtained based on the method proposed by

214   Wang et al. (2013).

215
$$D(t) = b * t^n + D_0 \tag{3}$$

216   in which, $D(t)$ is the colloidal effective diameter at time t (min), D_0 is the initial effective

217   diameter of colloids, and b and n are constants determined by the aggregation curves.

218   The fractal dimension is $d_f = 1/n$ in the DLA regime.

219 **3. Results and discussion**

3.1 Particle size and distribution characteristics of Anthrosol and Calcisol colloidal fractions

The average diameters of Anthrosol and Calcisol colloids were measured by time-resolved DLS, and the results were shown in Table 1. The number-weighted diameters for Anthrosol colloids of $d < 2$ μm were about 1.04 times of $d < 1$ μm, and about 1.84 times of d < 100 nm, respectively. The intensity-weighted diameters for Anthrosol colloids were 294.10~396.81 nm. For Calcisol colloidal fractions, the number-weighted diameters for colloids of $d < 2$ μm were about 1.07 times of $d < 1$ μm, and about 1.65 times of d < 100 nm, and the intensity-weighted diameters were 312.25~439.20 nm. The intensity-weighted diameters were generally higher than the number-weighted diameters, especially in polydisperse system (Xu et al., 2020b). The colloidal particles in the soil solution were in constant Brownian motion, upon illumination by light, these colloidal particles scatter light, causing variations in light intensity. This phenomenon allowed for the calculation of the effective diameter of the particles, which was the intensity-weighted diameter (Filella et al., 1997). Given that particle diameter is proportional to the sixth power of light intensity. Consequently, in polydisperse systems where larger particles were present, the number-weighted diameter provided typically a more accurate representation of the true diameter of colloidal particles (Xu et al., 2015).

(*Insert Table 1 near here*)

From table 1, it can be seen that the average colloidal diameters of $d < 2$ μm were close to that of $d < 1$ μm, and they were both significantly higher than that of the nano-

242　sized fraction. From the particle size distribution characteristics, it is clear that the size

243　range indicated by the differences of D_{90} and D_{10} increased with intended particle

244　diameter. For Anthrosol and Calcisol, 74.69% and 63.55% of all particles contained in

245　the colloidal suspensions of $d < 100$ nm were actually less than 100 nm, respectively,

246　indicating the complexity of soil colloidal particle irregularity.

247　**3.2 Physiochemical properties and clay mineralogy of Anthrosol and Calcisol**

248　　　**colloids**

249　　　Table 2 shows the physiochemical properties of soil colloidal fractions. The yields

250　of each colloidal fraction of Anthrosol were slightly larger than that of Calcisol,

251　respectively. The yields of colloidal particles of $d < 2$ μm were about 1.3~1.4 times of

252　$d < 1$ μm, and about 4.0~4.9 times of $d < 100$ nm, respectively. With the decreasing

253　colloidal particle diameter, the total carbon content, organic carbon and inorganic

254　carbon content all increased, suggesting the finer particles were richer in carbon. This

255　tendency is in agreement with other publications (Zhang et al., 2021; Said-Pullicino et

256　al., 2021; Hu et al., 2022). The specific surface areas for colloidal fractions of $d < 1$ μm

257　were largest of all, which may be related to the structures of formed clusters while

258　drying the samples for observation under microscopy (Yu et al., 2017; Weissenberger

259　et al., 2021). Furthermore, Anthrosol and Calcisol nanoparticles exhibited the lowest

260　specific surface area. This phenomenon raised from Organic substances adsorb

261　relatively little inorganic nitrogen (Li et al., 2013; Wilson et al., 2008). Therefore,

262　However, to our knowledge, no other better method has been reported for measuring

263　the specific surface area of natural nanoparticles.

264   (*Insert Table 2 near here*)

265   The clay mineralogy of Anthrosol and Calcisol colloidal fractions is shown in

266   Table 3. Calcisol colloidal fractions were dominant by illite, kaolinite and chlorite while

267   there was less chlorite in Anthrosol colloidal fractions. With the decrease of particle

268   size, the content of illite increased and kaolinite content decreased. This tendency is in

269   agreement with other publications (Chenu and Plante, 2006; Zhang et al., 2016). Among

270   the dominant clay types, the size of illite is finer than kaolinite and chlorite (Weil and

271   Brady, 2016), so its mass percentage was higher in the nano-sized fraction.

272   (*Insert Table 3 near here*)

273   **3.3 Surface properties of Anthrosol and Calcisol colloids**

274   The XPS spectra of soil colloidal fractions are shown in Fig. 1. From Fig. 1, it can

275   be seen that the main C-containing functional groups were C–C/C-H/C=C, C–O, C=O,

276   and COO- groups at 284.6, 286.2, 288.0 and 289.4 eV, respectively (Liang et al., 2020;

277   Ding et al., 2023). The functional groups for colloidal particles of $d < 100$ nm were

278   more abundant than those for colloids of $d < 2$ μm and $d < 1$ μm, while there were no

279   significant differences between colloids of $d < 2$ μm and $d < 1$ μm. With the decrease

280   of colloidal particle diameter, the relative contents of oxygen-containing functional

281   groups (C–O, C=O, COO-) gradually decreased. Specifically, the content decreased

282   gradually from 32.01% in Lou colloids of $d < 2$ μm to 20.93% in Lou colloids of $d <$

283   100 nm (Table S2). The functional groups of C–O and COO- gradually decreased until

284   they eventually disappeared, more C=O groups were exposed to the surrounding air.

285   For Calcisol colloids (Fig. 1d, e, f), the relative contents of organic oxygen-

286   containing functional groups for colloidal particles of $d < 2$ μm, $d < 1$ μm and $d < 100$

287   nm showed a different trend, compared with that in Anthrosol colloids. The relative

288   contents of organic oxygen-containing functional groups gradually increased with the

289   decrease of diameter. This trend was particularly pronounced in fraction of $d < 100$ nm,

290   and contents of C–O and COO- were highly increased (Table S2).

291   (*Insert Figure 1 near here*)

292   Oxygen-containing functional groups of C–O, C=O and COO- are electronegative

293   functional groups, hydroxyl and carboxyl groups can lose protons and make the surface

294   of soil colloidal particles carry negative charges (Audette et al., 2021). Functional

295   groups of C–O, C=O and COO- can affect the negative charges carried on the colloidal

296   surface by forming hydrogen bonds, and their polarity can also affect the negative

297   charges on the surface when O atom combines with C and H. The electrons will lean

298   towards the O atom with stronger electronegativity, which also makes the colloidal

299   surface carry negative charges (Tan et al., 2019). The contents and types of oxygen-

300   containing functional groups are one of the main factors affecting colloid charge and

301   aggregation.

302   The zeta potential values of different colloidal fractions at the pH range of 3–10

303   are shown in Fig. 2. Zeta potentials of the colloidal particles were negative, indicating

304   that they were negatively-charged. The zeta potentials of Anthrosol and Calcisol

305   colloidal particles were more negative with increasing solution pH, due to the

306   deprotonation of the surface (Moayedi and Kazemian, 2013; Dong et al., 2019).

307   Compared with the Calcisol colloids, the zeta potentials of Anthrosol colloidal particles

308   were more negative, due to Anthrosol possessed a higher surface charge density. For

309   Calcisol colloids, the differences among colloidal fractions were larger.

311   In general, zeta potential became more negative with increasing particle diameter.

312 When the pH changed from 3 to 10, for every pH unit increased, the zeta potential

313 values of Anthrosol colloids of $d < 2$ μm, < 1 μm, and < 100 nm would be increased by

314 2.14 mV, 2.09 mV and 1.89 mV; and for Calcisol colloids, those variation rates were

315 2.15 mV, 1.45 mV and 1.37 mV, respectively. Those data demonstrate that the charge

316 variability decreasing with the decreasing particle diameter. Song et al., (2019)

317 compared the zeta potential of wheat straw biochar nanoparticles (< 100 nm) and

318 colloidal particles (< 1000 nm), and found that the absolute values of colloidal particles

319 were larger at same pH, which was explained by the differences in the number of

320 surface carboxyl and hydroxyl groups. The zeta potential of colloidal particles is

321 proportional to charge density, which means that it is related to both charge quantity

322 and specific surface area (Hou et al., 2009). Therefore, the size effect of zeta potential

323 of Anthrosol and Calcisol colloidal particles is mainly related to the reduction of charge

324 density caused by larger specific surface area of nanoparticles (Xu et al. 2020b).

325 **3.4 Aggregation kinetics curves of Anthrosol and Calcisol colloids in NaCl and**

326 **CaCl$_2$ solutions**

327   The aggregation kinetics of Anthrosol and Calcisol colloids in NaCl and CaCl$_2$

328 solutions are shown in Figs. S1 and S2. The aggregation process of soil colloids was

329 divided into RLA and DLA stages. The RLA stages for Anthrosol colloids of $d < 2$ μm,

330 $d < 1$ μm and $d < 100$ nm in NaCl solution were 0–80, 0–80 and 0–100 mmol·L^{-1},

331 respectively, during which repulsive forces existed between the particles and

16

332   attachment did not occur on every collision. As the electrolyte concentration continued

333   to increase, the solution entered into the DLA regime. At this point, attachment occurred

334   with every collision between particles, and the aggregation rates were not affected by

335   the electrolyte concentration. At last, the effective diameters of the formed clusters were

336   stable at around 1600 nm. Figure S1b, d and f showed that the aggregation behaviors

337   of Anthrosol colloids in $CaCl_2$ solution were similar to that in NaCl solution, and the

338   corresponding $CaCl_2$ concentrations for Anthrosol colloids of $d < 2$ μm, $d < 1$ μm and

339    $d < 100$ nm in RLA stage were about 0–1.5, 0–1.5 and 0–2 mmol·L^{-1}, respectively.

340   The aggregation kinetics of Calcisol colloids in NaCl and $CaCl_2$ solutions were

341   similar to Anthrosol colloids (Fig. S2). The RLA stages for Calcisol colloids of $d < 2$

342   μm, $d < 1$ μm and $d < 100$ nm in NaCl solution were 0–100, 0–120 and 0–250 mmol·L^{-1},

343   and were about 0–1.8, 0–1.7 and 0–2 mmol·L^{-1} in $CaCl_2$ solution, respectively. The

344   effective diameters of the clusters for Calcisol colloids were stabilized at about 1600

345   nm and 1800 nm in NaCl and $CaCl_2$ solutions, respectively.

346   Aggregation rates of soil colloids varied with particle diameters at the same

347   electrolyte concentration, which was particularly evident in RLA stage (Table 4). With

348   decreasing particle diameter, the aggregation rates of Anthrosol and Calcisol colloids

349   in 50 mmol·L^{-1} NaCl and 1 mmol·L^{-1} $CaCl_2$ solutions exhibited a corresponding

350   decline. In addition, in 50 mmol·L^{-1} NaCl solution, the aggregation rates for Anthrosol

351   colloids of $d < 2$ μm, $d < 1$ μm and $d < 100$ nm were about 2.17, 2.09 and 1.95 times

352   those of Calcisol colloids, while the aggregation rates were about 1.46, 1.57 and 1.91

353   times those of Calcisol colloids in 1 mmol·L^{-1} $CaCl_2$ solution, respectively. Therefore,

from table 4, the aggregation rates of Anthrosol and Calcisol colloids showed the size

effect. From table 4, it could be observed that the fractal dimensions in NaCl solutions

were largely higher than those in $CaCl_2$ solutions, suggesting a much denser structure

(Meng et al., 2013). In other words, the formed structures in divalent solutions were

more open.

(Insert Table 4 near here)

3.5 Suspension stability of Anthrosol and Calcisol colloids in NaCl and CaCl₂ solutions

The CCCs for Anthrosol colloids of $d < 2$ μm, $d < 1$ μm and $d < 100$ nm in NaCl

solution were 80.40, 91.78 and 134.96 mmol·L^{-1}, respectively (Fig. 3a), and those for

Calcisol colloids were 121.10, 126.50 and 292.86 mmol·L^{-1}, respectively (Fig. 3b). The

CCCs increased with the decreasing particle diameter, indicating that the suspension

stability of soil nanoparticles was stronger than those of colloidal particles.

(Insert Figure 3 near here)

In $CaCl_2$ solutions, the CCCs for Anthrosol colloids of $d < 2$ μm, $d < 1$ μm and d

< 100 nm were 1.61, 1.68 and 1.77 mmol·L^{-1}, respectively, and for Calcisol colloids,

those corresponding values were 1.90, 1.91 and 2.13 mmol·L^{-1} (Fig. 4). The CCCs in

$CaCl_2$ solutions also increased with the decreasing particle size. The contents of K^+,

Na^+, Ca^{2+} and Mg^{2+} in Anthrosol and Calcisol colloidal suspensions decreased with the

decreasing colloidal particle diameter (Table S3), which was mainly due to the dilution

effect during the extraction process. Furthermore, Table S3 showed that the soluble

cation contents were rather low, and their effects on the CCCs of soil colloids could be

18

376 neglected.

377

378   Based on Figs. 3 and 4, 3 mmol$\cdot$L^{-1} CaCl$_2$ solution could cause fast aggregation

379 of soil colloidal particles, while it required at least 80 mmol$\cdot$L^{-1} NaCl solution for

380 comparable aggregation rate, indicating that the shielding effect of divalent cations on

381 negative charges of colloids was stronger than that of monovalent cations. The

382 quantitative calculation results showed that the CCC ratios of monovalent ion and

383 divalent ion system were between 25.64 and 27.09, which conformed to the Schulze-

384 Hardy rule (Baalousha, 2017).

385   For each type of the soil colloids, the higher the absolute zeta potential values of

386 colloidal particles, the more negative charges carried on the surface, and the higher the

387 stability (CCCs) of suspension. For the same particle diameter, e.g. $d < 100$ nm, the

388 absolute zeta potentials of Anthrosol colloids were larger (Fig. 2) while the

389 corresponding CCC was lower (Figs. 3 and 4). Study on the stability of biochar

390 nanoparticles showed that the absolute values of zeta potentials could not be used to

391 directly explain the stability difference among biochar nanoparticles from different

392 feedstock materials but could explain the influences of solution conditions on the

393 stability of biochar nanoparticles derived from the same feedstock material (Xu et al.,

394 2020a).

395   The CCCs of Anthrosol and Calcisol colloids increased with decreasing diameter;

396 that is, the CCCs of Anthrosol and Calcisol colloids both showed the size effects. Hsu

397 and Kuo (1995) demonstrated that the CCCs would generally decrease with the

increasing particle diameter because smaller particles possess thicker double electric layers and higher electrolyte concentration is needed to neutralize charges on the surface, which were consistent with the results of Anthrosol and Calcisol colloids. The above explanation by Hsu and Kuo (1995) was derived from homogenous particles whose composition does not change with particle diameter. The results of this paper show that, for those two alkaline soils being such heterogeneous materials, when the organic matter contents and mineral types changed with colloidal particle diameter, the CCCs in monovalent and divalent solutions also decreased with increasing particle diameter.

In this paper, the organic matter contents of soil nanoparticles were the highest, so the CCCs were the largest, which were 1.7 and 2.4 times of the corresponding colloidal particles of $d < 2$ μm. The suspension stability of different clay minerals has been reported to vary with the mineralogical structure. The CCC of illite ($\approx$100 mM) in NaCl solution was significantly higher than that of kaolinite ($\approx$20 mM) (Jiang et al., 2012; Xu et al., 2017), indicating that the stability of illite suspensions is significantly higher than that of kaolinite. So another possible reason for the higher stability of soil nanoparticles is the increase of illite content and the decrease of kaolinite content. Therefore, the differences in organic matter contents and clay mineralogy are the fundamental reasons for the differences in colloidal suspension stability behind the size effects of Anthrosol and Calcisol colloids.

4. Conclusion

This study obtained soil colloidal fractions with three different particle sizes from

Anthrosol and Calcisol using high-speed centrifugation and revealed the particle size effects on the soil constitutes, surface properties, and aggregation behavior of heterogeneous soil colloids. The results showed that, compared to coarse colloids ($d < 2$ μm and $d < 1$ μm), the organic carbon contents of Anthrosol and Calcisol nanoparticles were higher, at 27.38 g·kg^{-1} and 28.31 g·kg^{-1}, respectively, approximately twice and three times that of the coarse colloids and the bulk soils, indicating that nanoparticles exhibit a strong potential for carbon sequestration. The absolute zeta potential values of soil nanoparticles decreased with decreasing average particle diameter, indicating a reduction in charge density. Anthrosol and Calcisol nanoparticles exhibited greater suspension stability in NaCl and CaCl$_2$ solutions. On one hand, this was due to the increased thickness of the double electric layer on the surface of soil nanoparticles, resulting in stronger repulsive forces between particles; on the other hand, it was due to the presence of more illite, which has higher CCC compared to other clay minerals. In conclusion, for such a highly heterogeneous system as soil, the size effects on soil colloidal suspension stability are strongly influenced by variations driven by essentially mineral composition. Future studies should further explore the mechanisms underlying the size effects of the typical soils on particle interactions, coagulation, and transport behaviors under environmentally relevant conditions.

Acknowledgments

443

Author Contributions

445   Conceptualization, Xu, C.Y., Geng, Z.C., and Hu, F.N.; methodology, Xu, C.Y.;

446 software, Yan, Y.Y.; formal analysis, Liu, J.J.; investigation, Zhang, X.R.; resources,

447 Yan, Y.Y.; writing—original draft, Yan, Y.Y.; writing—review and editing, Xu, C.Y.,

448 and Hu, F.N.; visualization, Xu, C.Y., and Yan, Y.Y.; funding acquisition, Xu, C.Y.,

449 Geng, Z.C. and Hu, F.N.. All authors have read and agreed to the published version of

450 the manuscript.

451

Declaration of Interest Statement

453 The authors declare that they have no known competing financial interests or personal

454 relationships that could have appeared to influence the work reported in this paper.

455

References

457 Audette, Y., Congreves, K.A., Schneider, K., Zaro, G.C., Nunes, A.L.P., Nunes, A.L.P.,

458   Zhang, H.J., Voroney, R.P.: The effect of agroecosystem management on the

459   distribution of C functional groups in soil organic matter: A review. Biol. Fertil.

460   Soils. 57, 881–894, 2021.

461 Baalousha, M.: Aggregation and disaggregation of iron oxide nanoparticles: Influence

462   of particle concentration, pH and natural organic matter. Sci. Total Environ. 407(6),

463   2093–2101, 2009.

464   Baalousha, M.: Effect of nanomaterial and media physicochemical properties on

465   nanomaterial aggregation kinetics. NanoImpact. 6, 55–68, 2017.

466   Cárdenas, J.P., Santiago, A., Tarquis, A.M., Losada, J.C., Borondo, F., Benito, R.M.:

467   Soil porous system as heterogeneous complex network. Geoderma. 160(1), 13–21,

468   2010.

469   Chenu, C., Plante, A.F.: Clay-sized organo-mineral complexes in a cultivation

470   chronosequence: revisiting the concept of the 'primary organo-mineral complex'.

471   Eur J Soil Sci. 57(4), 596–607, 2006.

472   Ding, W., Liang, H.X., Zhang, H.W., Sun, H., Geng, Z.C., Xu, C.Y.: A

473   cellulose/bentonite grafted polyacrylic acid hydrogel for highly-efficient removal

474   of Cd(II). J. Water Process. Eng. 51, 103414, 2023.

475   Dong, S.N., Zeng, Z., Cai, W.W., Zhou, Z.Y., Dou, C.B., Liu, H., Xia, J.H.: The zeta

476   potentials of g-C_3N_4 nanoparticles: Effect of electrolyte, ionic strength, pH, and

477   humic acid. J. Nanopart Res. 21, 233, 2019.

478   Filella, M., Zhang, J.W., Newman, M.E., Buffle, J.: Analytical applications of photon

479   correlation spectroscopy for size distribution measurements of natural colloidal

480   suspensions: capabilities and limitations. Colloid Surf. A. 120(1–3), 27–46, 1997.

481   He, Y.T., Wan, J., Tokunaga, T.: Kinetic stability of hematite nanoparticles, The effect

482   of particle sizes. J. Nanopart Res. 10, 321–332, 2008.

483   Hou, J., Li, H., Zhu, H.L.,Wu, L.S.: Determination of clay surface potential, a more

484   reliable approach. Soil Sci Soc Am J. 73(5), 1658–1663, 2009.

485   Hsu, J.P., Kuo, Y.C.: An Extension of the Schulze-Hardy Rule to Asymmetric

486   Electrolytes. J. Colloid Interface Sci. 171(1), 254–255, 1995.

487   Hu, N., Xu, C.Y., Geng, Z.C., Hu, F.N., Li, Q.R., Ma, R.T., Wang, Q.: The interplay of

488   particle properties and solution chemistry on aggregation kinetics of soil

489   nanoparticles. J Soils Sediments. 22, 1761–1772, 2022.

490   IUSS Working Group WRB. World Reference Base for Soil Resources. International

491   soil classification system for naming soils and creating legends for soil maps. 4th

492   edition. International Union of Soil Sciences (IUSS), Vienna, Austria. 2022.

493   Jiang, C.L., Séquaris, J.M., Vereecken, H., Klumpp, E.: Effects of inorganic and organic

494   anions on the stability of illite and quartz soil colloids in Na-, Ca- and mixed Na-

495   Ca systems. Colloids Surf. A. 415, 134–141, 2012.

496   Lead, J.R., Wilkinson, K.J.: Aquatic Colloids and Nanoparticles: Current Knowledge

497   and Future Trends. Environ. Chem. 3(3), 159–171, 2006.

498   Li, S.X., Luo, Y.M., Zhang, H.B., Huang, Y.J., Li, Z., Wei, J.: Arsenic forms in various

499   particle-size fractions of red soil-Chemical fractionation and speciation using

500   XANES analysis. Acta Scientiae Circumstantiae. 31(12), 2733–2739, 2011.

501   Li, W. Y., Zhu, X.Y., He, Y., Xing, B. S., Xu, J.M.: Enhancement of water solubility and

502   mobility of phenanthrene by natural soil nanoparticles. Environ Pollut. 176, 228–

503   233, 2013.

504   Liang, H.X., Sun, R.R., Song, B., Sun, Q.Q., Peng, P., She, D.: Preparation of nitrogen-

505   doped porous carbon material by a hydrothermal-activation two-step method and

its high-efficiency adsorption of Cr(VI). J. Hazard. Mater. 387, 121987, 2020.

Luo, J.J., Niu, Q., Jin, M.C., Cao, Y.A., Ye, L.R., Du, R.P.: Study on the effects of oxygen-containing functional groups on Hg^0 adsorption in simulated flue gas by XAFS and XPS analysis. J. Hazard. Mater. 376(15), 21–28, 2019.

Mayordomo, N., Degueldre, C., Alonso, U., Missana, T.: Size distribution of FEBEX bentonite colloids upon fast disaggregation in low-ionic strength water. Clay Miner. 51(2), 213–222, 2016.

Meng, Z.Y., Hashmi, S.M., Elimelech, M.: Aggregation rate and fractal dimension of fullerene nanoparticles via simultaneous multiangle static and dynamic light scattering measurement. J. Colloid Interface Sci. 392, 27–33, 2013.

Moayedi, H., Kazemian, S.: Zeta potentials of suspended humus in multivalent cationic saline solution and its effect on electro-osomosis behavior. J. Dispers Sci. Technol. 34(2), 283–294, 2013.

Said-Pullicino, D., Giannetta, B., Demeglio, B., Missong, A., Gottselig, N., Romani, M., Bol, R., Klumpp, E., Celi, L.: Redox-driven changes in water-dispersible colloids and their role in carbon cycling in hydromorphic soils. Geoderma. 385, 114894, 2021.

Schäfer, T., Huber, F., Seher, H., Missana, T., Alonso, U., Kumke, M., Eidner, S., Claret, F., Enzmann, F.: Nanoparticles and their influence on radionuclide mobility in deep geological formations. Appl. Geochemistry. 27(2), 390–403, 2012.

Song, B.Q., Chen, M., Zhao, L., Qiu, H., Cao, X.D.: Physicochemical property and colloidal stability of micron- and nano-particle biochar derived from a variety of

528   feedstock sources. Sci. Total Environ. 661, 685–695, 2019.

529   Sun, Y.L., Pan, D.Q., Wei, X.Y., Xian, D.F., Wang, P., Hou, J.J.: Insight into the stability

530   and correlated transport of kaolinite colloid: Effect of pH, electrolytes and humic

531   substances. Environ. Pollut. 266, 115189, 2020.

532   Tan, Z.X., Yuan, S.N., Hong, M.F., Zhang, L.M., Huang, Q.Y.: Mechanism of negative

533   surface charge formation on biochar and its effect on the fixation of soil Cd. J.

534   Hazard. Mater. 384, 121370, 2019.

535   Tang, Y., Li, H., Liu, X.M., Zhu, H.L., Tian, R.: Unraveling the size distributions of

536   surface properties for purple soil and yellow soil. J Environ Sci (China). 32, 81–

537   89, 2015.

538   Tsao, T.M., Chen, Y.M., Sheu, H., Tzou, Y.M., Chou, Y.M., Wang, M.K.: Separation

539   and identification of soil nanoparticles by conventional and synchrotron X-ray

540   diffraction. Appl. Clay Sci. 85, 1–7, 2013.

541   Tsao, T.M., Chen, Y.M., Wang, M.K., Huang, P.M.: Structural transformation and

542   physicochemical properties of environmental nanoparticles by comparison of

543   various particle-size fractions. Soil Sci Soc Am J. 75(2), 533–541, 2011.

544   Wang, L.F., Wang, L.L., Ye, X.D., Li, W.W., Ren, X.M., Sheng, G.P., et al.: Coagulation

545   kinetics of humic aggregates in mono-and divalent electrolyte solutions. Environ.

546   Sci. Technol. 47(10), 5042–5049, 2013.

547   Wang, Q.R., Li, Y.C., Wang, Y.: Optimizing the weight loss-on-ignition methodology

548   to quantify organic and carbonate carbon of sediments from diverse sources.

549   Environ. Monit. Assess. 174, 241–257, 2011.

550 Wei, X.Y., Pan, D.Q., Xu, Z., Xian, D.F., Li, X.L., Tan, Z.Y., Liu, C.L., Wu, W.S.:

551 Colloidal stability and correlated migration of illite in the aquatic environment:

552 The roles of pH, temperature, multiple cations and humic acid. Sci. Total Environ.

553 768, 144174, 2021.

554 Weil, R.R., Brady, N.C.: The Nature and Properties of Soils, Global Edition. Pearson

555 Education Limited. 2016.

556 Weissenberger, G., Henderikx, R.J., Peters, P.J.: Understanding the invisible hands of

557 sample preparation for cryo-EM. Nat. Methods. 18(5), 463–471, 2021.

558 Wilson, M. A., Tran, N. H., Milev, A. S., Kannangara, G. S. K., Volk, H.: Nanomaterials

559 in soils. Geoderma. 146, 291–302, 2008.

560 Won, J., Burns, S.E.: Role of Immobile Kaolinite Colloids in the Transport of Heavy

561 Metals. Environ. Sci. Technol. 52(5): 2735–2741, 2018.

562 Xu, C.Y., Deng, K.Y., Li, J.Y., Xu, R.K.: Impact of environmental conditions on

563 aggregation kinetics of hematite and goethite nanoparticles. J. Nanopart Res. 17,

564 394, 2015.

565 Xu, C.Y., Li, Q.R., Geng, Z.C., Hu, F.N., Zhao, S.W.: Surface properties and suspension

566 stability of low–temperature pyrolyzed biochar nanoparticles: Effects of solution

567 chemistry and feedstock sources. Chemosphere. 259, 127510, 2020a.

568 Xu, C.Y., Xu, R.K., Li, J.Y., Deng, K.Y.: Phosphate-induced aggregation kinetics of

569 hematite and goethite nanoparticles. J. Soils Sediments. 17, 352–363, 2017.

570 Xu, C.Y., Zhou, T.T., Wang, C.L., Liu, H.Y., Zhang, C.T., Hu, F.N., Zhao, S.W., Geng,

571 Z.C.: Aggregation of polydisperse soil colloidal particles: Dependence of

Hamaker constant on particle size. Geoderma. 359, 113999, 2020b.

Xu, Z., Pan, D.Q., Sun, Y.L., Wu, W.S.: Stability of GMZ bentonite colloids: Aggregation kinetic and reversibility study. Appl. Clay Sci. 161, 436–443. 2018.

Yin, X.Q., Gao, B., Ma, L.Q., Saha, U.K., Sun, H.M., Wang, G.D.: Colloid-facilitated Pb transport in two shooting-range soils in Florida. J. Hazard. Mater. 177(1–3), 620–625, 2010.

Yu, X., Fu, Y., Lu, S.: Characterization of the pore structure and cementing substances of soil aggregates by a combination of synchrotron radiation X-ray micro–computed tomography and scanning electron microscopy. Eur. J. Soil Sci. 68(1), 66–79, 2017.

Zhang, Q., Bol, R., Amelung, W., Missong, A., Siemens, J., Mülder, I.: Water dispersible colloids and related nutrient availability in Amazonian Terra Preta soils. Geoderma. 397, 115103, 2021.

Zhang, Z.Y., Huang, L., Liu, F., Wang, M.K., Fu, Q.L., Zhu, J.: Characteristics of clay minerals in soil particles of two Alfisols in China. Appl. Clay Sci. 120, 51–60, 2016.

Zhou, D.X., Ji, Z.X., Jiang, X.M., Dunphy, D.R., Brinker, J., Keller A.A.: Influence of material properties on TiO_2 nanoparticle agglomeration. PLoS One. 8(11), e81239, 2013.

Zhu, X., Chen, H., Li, W., He, Y., Brookes, P.C., Xu, J.: Aggregation kinetics of natural soil nanoparticles in different electrolytes. Eur. J. Soil Sci. 65(2), 206–217, 2014.

595 **Table captions**

596 **Table 1** The average diameters and distribution patterns of soil colloids.

597 **Table 2** The physiochemical properties of soil colloids.

598 **Table 3** The dominant clay minerals of soil colloidal fractions (shown in mass

599 fraction, %).

600 **Table 4** The aggregation rates of soil colloids.

601

602   **Table 1** The average diameters and distribution patterns of soil colloids

Soil type	Colloidal fractions	Number-weighted diameter (nm)	Intensity-weighted diameter (nm)	D_{10} (nm)	D_{90} (nm)
	$d < 2$ μm	133.16 ± 24.28	396.81 ± 12.34	71.53	232.49
Anthrosol	$d < 1$ μm	127.84 ± 20.29	371.45 ± 11.88	67.64	219.87
	$d < 100$ nm	72.47 ± 7.04	294.10 ± 15.80	38.74	136.72
	$d < 2$ μm	141.23 ± 24.33	439.20 ± 12.72	78.29	244.97
Calcisol	$d < 1$ μm	131.67 ± 15.77	372.07 ± 8.23	75.84	231.64
	$d < 100$ nm	85.48 ± 16.93	312.25 ± 33.58	47.84	158.99

603   Note: D_{10}, D_{50} and D_{90} represent diameter of particles with a cumulative distribution of 10%, 50% and
604   90%, respectively.

605

Table 2 The physiochemical properties of soil colloids

Soil type	Colloidal fractions	Yield (%)	Total carbon content (g·kg^{-1})	Organic carbon content (g·kg^{-1})	CaCO$_3$ content (g·kg^{-1})	Specific surface area (m^2·g^{-1})
	$d < 2$ μm	25.12	20.90 ± 0.30	10.90 ± 1.29	10.00	65.37
Anthrosol	$d < 1$ μm	18.76	20.65 ± 0.15	10.91 ± 0.43	9.74	72.99
	$d < 100$ nm	6.32	58.25 ± 0.35	27.38 ± 0.21	30.87	45.28
	$d < 2$ μm	23.17	24.00 ± 0.30	11.66 ± 0.60	12.34	49.99
Calcisol	$d < 1$ μm	16.20	22.30 ± 0.20	12.76 ± 0.11	9.54	61.88
	$d < 100$ nm	4.70	76.30 ± 0.40	28.31 ± 0.15	47.99	34.53

608 **Table 3** The dominant clay minerals of soil colloidal fractions (shown in mass fraction, %)

Soil type	Colloidal fractions	Illite	Kaolinite	Chlorite	Vermiculite
Anthrosol	$d < 2$ μm	34	23	4	9
	$d < 1$ μm	30	22	7	11
	$d < 100$ nm	37	14	16	3
Calcisol	$d < 2$ μm	24	22	29	16
	$d < 1$ μm	31	19	25	12
	$d < 100$ nm	37	16	17	5

609

610

Table 4 The aggregation rates of soil colloids

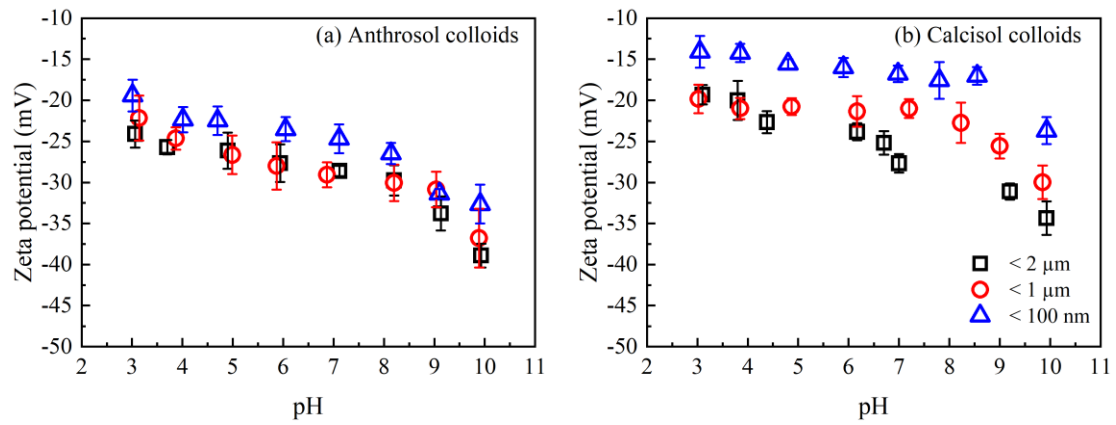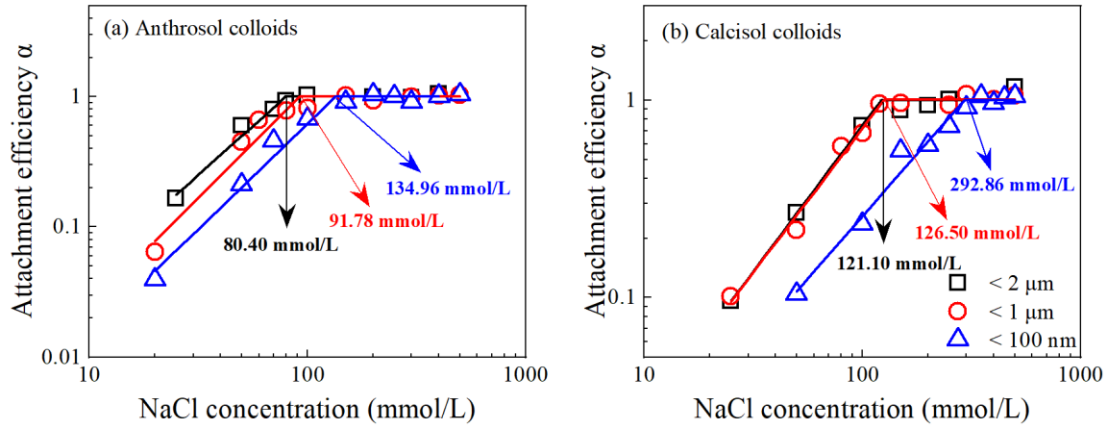| Soil type	Colloidal fractions	Aggregation rate		Fractal dimension	
		In 50 mmol·L^{-1} NaCl (nm·min^{-1})	In 1 mmol·L^{-1} CaCl$_2$ (nm·min^{-1})	Na	Ca
Anthrosol	$d < 2$ μm	19.46	12.01	1.69 ± 0.19	1.33 ± 0.26
	$d < 1$ μm	14.91	11.48	1.75 ± 0.06	1.52 ± 0.19
	$d < 100$ nm	7.72	9.97	1.71 ± 0.26	1.68 ± 0.13
Calcisol	$d < 2$ μm	8.98	8.22	1.30 ± 0.17	1.36 ± 0.17
	$d < 1$ μm	7.15	7.33	1.71 ± 0.24	1.30 ± 0.31
	$d < 100$ nm	3.95	5.22	1.52 ± 0.22	1.58 ± 0.19

611

Figure captions

612

613 **Fig. 1.** The photoelectron spectrum C1s and O1s peak diagram of Anthrosol and

614 Calcisol colloids. C1s of Anthrosol colloids, a. $d < 2$ μm, b. $d < 1$ μm, c. $d < 100$ nm;

615 C1s of Calcisol colloids, d. $d < 2$ μm, e. $d < 1$ μm, f. $d < 100$ nm; O1s of Anthrosol

616 colloids, g. $d < 2$ μm, h. $d < 1$ μm, i. $d < 100$ nm; O1s of Calcisol colloids, j. $d < 2$ μm,

617 k. $d < 1$ μm, l. $d < 100$ nm.

618 **Fig. 2.** The zeta potential of Anthrosol (a) and Calcisol (b) colloids of $d < 2$ μm, < 1 μm,

619 and < 100 nm at different pH

620 **Fig. 3.** The CCCs of Anthrosol (a) and Calcisol (b) colloids of $d < 2$ μm, < 1 μm, and $<$

621 100 nm in NaCl solution

622 **Fig. 4.** The CCC of Anthrosol (a) and Calcisol (b) colloids of $d < 2$ μm, < 1 μm, and $<$

623 100 nm in CaCl2 solution
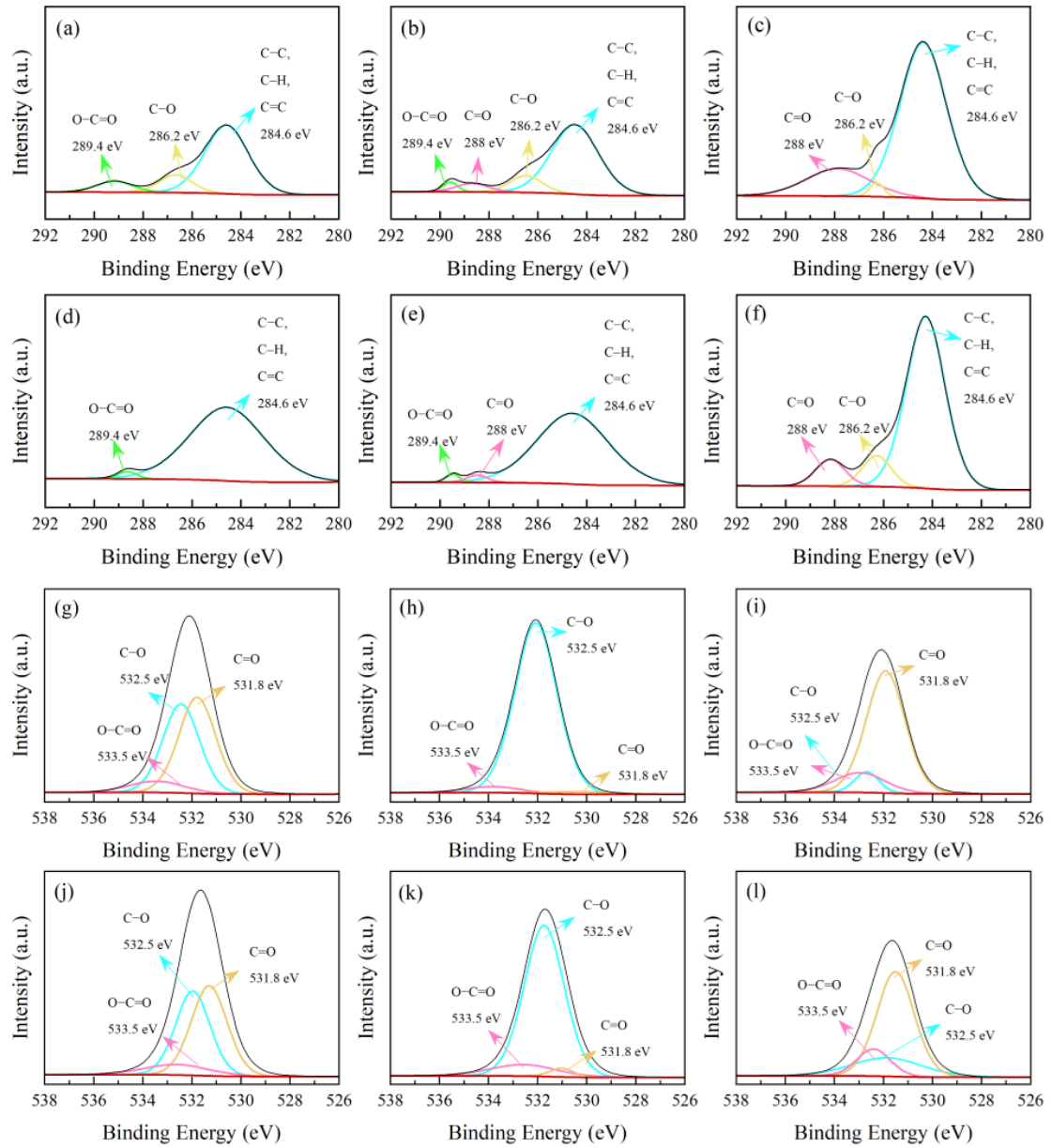
Fig. 1 The photoelectron spectrum C1s and O1s peak diagram of Anthrosol and Calcisol colloids. C1s of Anthrosol colloids, (a). $d < 2$ μm, (b). $d < 1$ μm, (c). $d < 100$ nm; C1s of Calcisol colloids, (d). $d < 2$ μm, (e). $d < 1$ μm, (f). $d < 100$ nm; O1s of Anthrosol colloids, (g). $d < 2$ μm, (h). $d < 1$ μm, (i). $d < 100$ nm; O1s of Calcisol colloids, (j). $d < 2$ μm, (k). $d < 1$ μm, (l). $d < 100$ nm.

631

Fig. 2 The zeta potential of Anthrosol (a) and Calcisol (b) colloids of d < 2 μm, < 1 μm, and < 100 nm at different pH
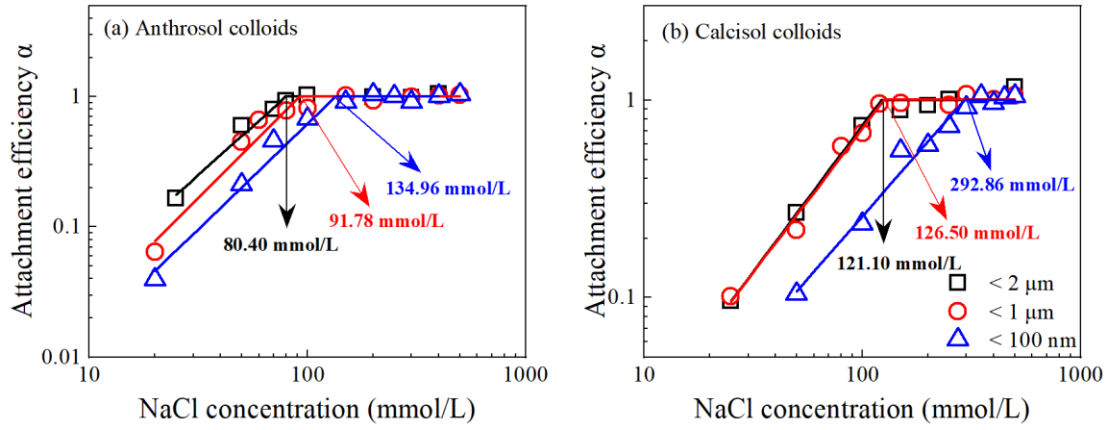
634

Fig. 3 The CCCs of Anthrosol (a) and Calcisol (b) colloids of d < 2 μm, < 1 μm, and < 100 nm in NaCl solution

Fig. 4 The CCC of Anthrosol (a) and Calcisol (b) colloids of $d < 2$ μm, < 1 μm, and < 100 nm in CaCl$_2$ solution。